Cooperative Binding of 1-Phenylimidazole to Cobalt(II) Octaethylporphyrin on Graphite: A Quantitative Imaging and Computational Study at Molecular Resolution [J Phys. Chem C 2020]

Katalin V. Korpany, Bhaskar Chilukuri, K. W. Hipps,* and Ursula Mazur*

Department of Chemistry, Washington State University, Pullman, Washington 99164-4630, United States

ABSTRACT: Cooperative interactions play a critical role in the stability and reactivity of biological systems and an increasingly important consideration in the synthesis of functional materials, but quantitative single-molecule measurements of this phenomenon are rare. Many of these cooperative interactions necessarily occur at surfaces, making the study of cooperative effects at interfaces of particular importance. Here we report a quantitative experimental and theoretical study of the cooperative binding of 1-phenylimidazole (PhIm) to cobalt(II) octaethylporphyrin (CoOEP) on highly oriented pyrolytic graphite (HOPG) at the solution-solid interface. Scanning tunneling microscopy (STM) confirmed and monitored the binding of PhIm to HOPG-supported CoOEP with single-molecule resolution. Nearest-neighbor analysis of these STM images revealed positive cooperative binding behavior. Periodic plane-wave density functional theory (DFT) calculations of PhIm/CoOEP/HOPG and cobalt(II) porphine (CoP)/HOPG systems support the experimental observations of positive cooperativity. DFT calculations revealed that the binding energy of PhIm to Co-porphyrin increases as PhIm binds to more neighboring molecules. Calculations also suggest that the presence of HOPG is crucial to observe positive cooperativity in this system.

INTRODUCTION

Cooperativity is an emergent property of a system, broadly characterized by a non-additivity of interactions. Cooperative interactions are abundant in biological systems, where they can alter stability and reactivity of interacting components, accelerate processes, and enhance detection sensitivity while decreasing noise.1,2 A classic example of cooperativity is the allosteric regulation of binding affinity, as observed in oxygen binding to hemoglobin.3 Less appreciated are the cooperative effects that underpin chelation,4 long-range protein communication,5 protein folding,6 and self-assembly.7 When considering cooperativity in ligand binding, positive cooperativity is indicated by an increase in binding affinity of subsequent molecules after the initial binding event, whereas negative cooperativity is observed as a decrease in the binding affinity for additional ligands. 1,6 Constraining and pre-organizing molecules on surfaces is another cooperative strategy employed by nature and functional materials synthesis to facilitate and regulate reactions and interactions through co-localization, and can allow cooperative interactions to propagate with substrate assistance.6,8-11

While many experimental studies¹⁻¹¹ show the qualitative existence of cooperative phenomena, quantitative measurements of cooperativity are quite rare due to numerous challenges involved in quantifying such phenomenon experimentally.¹² Alternatively, quantum mechanical simulations were widely used to study and understand cooperativity at the molecular level. For example, Rong et al.^{13,14} showed the application of DFT calculations to quantify cooperativity in various molecular systems. Vijay et

al. \$^{15}\$ studied the cooperativity of cation-\$\pi\$ and hydrogen bonding using quantum mechanical calculations. Cooperativity in water clusters was studied by Perez et al. \$^{16}\$ using rotational spectroscopy and quantum mechanical calculations. All these studies show that computational methods like DFT can be used to study cooperativity. A review \$^{17}\$ by Mahadevi and Sastry presents a collection of various studies of cooperativity caused by non-covalent interactions. They show the application of quantum chemical methods to study, understand and quantify cooperativity in multiple molecular systems involving various interactions ranging from hydrogen bonding, \$\pi\$-\$\pi\$ interactions, self-assembly, to charged species, with applications in fields like catalysis, supramolecular chemistry, self-assembly and biology.

Molecular level control and regulation of interactions is critical in materials synthesis. Of great interest is characterizing and controlling the binding of ligands to metal centers, given their rich chemistry and prevalence in natural systems and functional materials. Of these ligands, imidazole and other imidazole derivatives form a group of nitrogen bases that have high affinity for metals. 18,19 One of the most popular protein purification methods, IMAC (immobilized metal-affinity chromatography), relies on the binding of histidine and imidazole to metal-immobilized resins.²⁰ Metallated tetrapyrroles are ubiquitous as catalytic centers in enzymes and reaction centers for energy harvesting and electron transport.²¹ Hemoglobin, myoglobin, cytochrome c, vitamin B12, and cytochrome c oxidase are examples of proteins, protein complexes, or molecules that rely on metalloporphyrins or their analogs for their function.^{21,22} For these specific examples, axial coordination by histidine to the metal center via its sidechain imidazole is critical for molecular stability or function. ²²⁻²⁵ Imidazoles can also inhibit enzyme function. ¹-phenylimidazole belongs to a set of imidazoles and other azoles that strongly coordinate to the heme of cytochrome P450, effectively impeding its activity. ^{26,27}

Porphyrins have demonstrated significant potential as active components in sensors, artificial enzymes and oxygen carriers, for water splitting, and catalysis.^{28–32} For many of these applications, porphyrins will require deposition on supports and the influence of surface interactions on ligand binding must be considered. In some cases, surfaces can act as an additional axial ligand to the metal ion, affecting both porphyrin reactivity and surface stability.^{33–35} The binding reactions of O₂ to cobalt and copper octaethylporphyrin (OEP)^{36,37} and imidazole to nickel OEP³⁸ all necessitated charge donation from the underlying graphite support to occur, while the catalytic activity of cobalt tetraphenylporphyrin (Co-TPP) for the reduction of NO by CO was enhanced by almost two orders of magnitude after depositing Co-TPP on TiO₂.³⁹

Porphyrins can also serve to model reactions on a simpler scale.⁴⁰ Of these, octaethylporphyrins (OEP) represent a set of simple, compact, and highly studied porphyrins that form stable monolayers on a variety of metal surfaces and highly oriented pyrolytic graphite (HOPG).^{32,41,42} Metallated OEPs (MOEP) have been shown to bind a variety of ligands in solution,⁴³ the solid state,^{44,45} and on surfaces.^{36–38,46,47} Although the binding of imidazole and imidazole derivatives to metalloporphyrins has been previously demonstrated,^{48–56} few studies have reported the binding of these molecules to MOEPs,^{43–45,57} with only one showing imidazole binding to a surface-supported OEP.³⁸

A small fraction of all porphyrin ligand binding studies have been conducted with molecular resolution.33-^{38,40,46,47,58,59} Typically, ensemble measurements are used to examine these systems. Single-molecule techniques can follow reactions on a per-molecule basis in real-time. As a result, the identification and distribution of reactive sites. reaction mechanisms, and binding dynamics can be determined—details that might otherwise get lost in ensemble averaging. Scanning tunneling microscopy (STM) is particularly well suited to the study of molecular reactions on surfaces by offering both molecular resolution and information regarding changes in the electronic structure of materials upon reaction. 60,61 More realistic reaction conditions can be modeled, as STM samples can be characterized in solution with control over temperature and atmosphere. STM can be used to examine ligand binding cooperativity on surfaces on a per molecule basis. For example, the oxygen binding and oxidation reactions of manganese porphyrins on HOPG,40 Ag(111),35 and Au(111)34 show a preference for pairwise binding and reaction of adjacent porphyrins when experimental STM observations are compared to theoretical random distributions or simulated

To investigate cooperativity on surfaces in a relevant and simple system, we examined the ligand binding behavior of 1-phenylimidazole (PhIm) (Figure 1A) to surface-supported CoOEP (Figure 1A) in phenyloctane. Figure 1B shows a model of the complete complex. STM was used to

observe and confirm the binding reaction on a molecular scale, which allowed for an analysis of binding dynamics and the determination of PhIm-CoOEP adduct distribution. Using the experimental distribution of PhIm-bound CoOEP, with support from DFT calculations, we demonstrate the existence of positive cooperativity in PhIm binding to CoOEP.

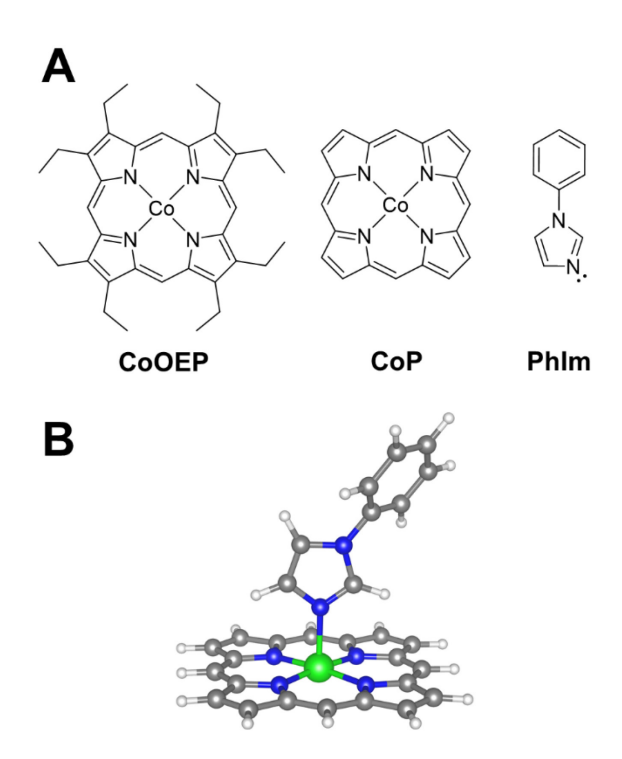


Figure 1. A) Molecular structures of cobalt(II) octaethylporphyrin (CoOEP), cobalt(II) porphine (CoP), and 1-phenylimidazole (PhIm). B) Molecular model of PhIm bound to CoP. Atom colors: Cobalt-green, porphyrin and PhIm carbons-grey, nitrogen-blue, hydrogen-white.

EXPERIMENTAL SECTION

Materials. 2,3,7,8,12,13,17,18-octaethyl-21H,23H-porphine cobalt(II) (CoOEP) and 1-phenylimidazole (PhIm; 97%) were purchased from Sigma-Aldrich (St. Louis, MO, USA). 1-Phenyloctane (>98.0%) was obtained from TCI America (Portland, OR, USA). Toluene (ACS grade or J.T. Baker, Ultra Resi-Analyzed) was obtained from Fisher Scientific (Waltham, MA, USA). All chemicals were used without further purification. Highly oriented pyrolytic graphite (HOPG) substrates used were 1 cm² in size and obtained from SPI (grade 2; West Chester, PA, USA) or TipsNano Co (ZYA quality; Tallinn, EE). STM tips were mechanically cut from Pt/Ir wire (California Fine Wire Co., Grover Beach, CA, USA; 80:20 Pt/Ir, 0.011-inch diameter).

STM Sample Preparation and Imaging. Solutions of 10 μM CoOEP were prepared by dissolving solid CoOEP in phenyloctane. A stock solution of 20 mM PhIm was prepared by diluting 25.3 μL of 1-phenylimidazole (a liquid at room temperature (RT), mp = 13 °C, d = 1.14 g/mL, MW = 144.17 g/mol) with toluene in a clean and oven-dried 10 mL volumetric flask, inverting several times to mix. Both

CoOEP and PhIm solutions were stored in the dark, in foil, at RT, and parafilmed until use.

All STM images were obtained in constant current mode using a Molecular Imaging (now Agilent Technologies Inc.) PicoSPM equipped with a 1 μ m STM scanner and environmental chamber (which allows for a controlled atmosphere). STM images were acquired using bias voltages ranging from +0.400 to +0.900 V and a setpoint current of 10 or 20 pA.

To prepare samples for STM imaging, an aliquot of the prepared 20 mM PhIm stock solution was diluted to 50 µM PhIm by serial dilution in toluene, followed by a final dilution to 10 µM with phenyloctane. The final solution composition of the 10 µM PhIm was 80% phenyloctane/20% toluene. 10 µL of 10 µM CoOEP was deposited on freshly cleaved HOPG in a custom-made solution cell fitted with a Kalrez o-ring (McMaster-Carr, Elmhurst IL, USA). The resulting sample was placed in the environmental chamber, and the chamber purged with 2.5 standard cubic feet per hour (scfh) Ar(g) for 10 min. After purging, Ar(g) flow was reduced to 0.5 scfh and was maintained at this rate throughout the experiment. STM imaging of the deposited CoOEP on HOPG was performed to confirm monolayer formation, then 10 µL of the above prepared 10 µM PhIm was added to the solution cell and the solutions mixed by gentle pipetting. The sample was allowed to equilibrate for at least 30 min before further imaging. The final sample composition was 1:1 CoOEP/PhIm in 90% phenvloctane/10% toluene. In order to ensure that the addition of PhIm did not introduce oxygen into the cell, blank solvent experiments were performed.

Image Analysis and Statistics. STM image analysis was carried out using Gwyddion v2.55 (Czech Metrology Institute, Brno, CZ) and SPIP (Image Metrology A/S, Lyngby, DK). Some images were denoised to improve clarity and aid identification of ligand-bound molecules. Denoising was performed as outlined in Oliveira et al.⁶² using Gwyddion and Python code for the sparse denoise module provided at http://www.lx.it.pt/~jpaos/stm/stm_code.html.

Experimental data for calculating the fraction of dark molecules and dark nearest neighbors was obtained by a combination of manual and programmatically assisted counting of STM images as outlined in the Supporting Information (Sections 1.1, 1.2). Typically, 50 nm \times 50 nm STM images were used, which contained on average $\sim\!1600$ surface adsorbed CoOEP molecules each. Theoretical k-nearest neighbor distributions and ratios of experimental and theoretical fractions of k-dark nearest neighbors were determined as outlined in the Supporting Information (Sections 1.2, 1.3).

Edge effects were considered. A square grid with 1600 points was randomly assigned occupation at various levels representing sample coverage and nearest neighbor analysis was performed. This was repeated 1000 times. The resulting averages were compared to the distribution expected for a random system. For coverages in the region where our experiments were performed, the total error in each of the distribution numbers was less than 5%. This analysis is an over-estimate of the role of edge effects.

UV-Visible Absorption Spectroscopy. All spectra were acquired on an Evolution 260 Bio spectrophotometer (Thermo Scientific, Waltham, MA, USA) using Tefloncapped 1 cm pathlength quartz cuvettes from 350–600 nm. CoOEP and PhIm were prepared as solutions in toluene. A reference spectrum of 5.9 μ M CoOEP was collected, then 64 μ L of 790 μ M PhIm was added to the CoOEP in the cuvette to obtain a \sim 9:1 solution ([PhIm] = 50 uM, [CoOEP] = 5.5 μ M). The solution was mixed by inversion and vortexing then allowed to equilibrate for 40 min prior to spectrum acquisition.

Computational Methods. All computations are performed with periodic density functional theory (DFT) using Vienna Ab-initio Simulation Package (VASP)63,64 version 5.4.4. The VASP code uses the projector augmented wave (PAW) method⁶⁵⁻⁶⁷ to describe the core electrons and valence-core interactions. We used optB88-vdW functional⁶⁸⁻⁷⁰ with PAW potentials optimized for the PBE functional⁷¹ for all calculations. The electronic wavefunctions are sampled using a Gamma (Γ) point in the irreducible Brillouin zone (BZ) using the Monkhorst and Pack (MP)⁷² method. A plane wave cut off energy of 550 eV was used for all simulations. Methfessel-Paxton smearing was used to set the partial occupancies for each wave function with a smearing width of 0.2 eV. All the geometries were fully optimized up to ~ 0.001 eV energy convergence. The choice of our DFT methodology, plane wave cutoff energies and kpoint choice was based on previous periodic DFT simulations of similar systems of type^{38,73-76} and size.⁷⁷ Additional computational details are presented in section 3 of the Supporting Information.

RESULTS AND DISCUSSION

Binding of PhIm to CoOEP. Before the addition of PhIm to the system, CoOEP was deposited on HOPG and a monolayer was confirmed by STM imaging to spontaneously form (Supporting Information, Figure S1). CoOEP organized as a pseudo-hexagonal lattice on HOPG, consistent with previous results.³⁶ Bright features in the images are similar to those observed in prior reports,³⁶ of un-ligated CoOEP molecules. After PhIm was added, a population of darker molecules arose over time which we infer to be the PhIm-CoOEP adduct. A representative image of the solution/CoOEP/HOPG interface after PhIm has been added is presented in Figure 2A. Images were typically acquired at positive bias voltages ranging from +0.400-0.900 V and 10 pA setpoint in order to maximize contrast between the ligand-adduct and un-ligated CoOEP. A cross-section over a sample of molecules (Figure 2C) further supports the presence of two primary species in the images. Previous work has shown that $O_2(g)$ can also bind to CoOEP on HOPG,³⁶ also producing molecules that appear dark under STM imaging. To prevent this contribution to binding, our experiments were carefully performed under argon atmosphere.

The binding of PhIm to CoOEP does not appear to influence the stability of the CoOEP monolayer at the ligand concentration used. The monolayer remained intact and presence of the adduct was observed through the imaging process, with repeated imaging, and over several days (Supporting Information, Figure S2). However, PhIm binding to the CoOEP does appear to be dynamic and reversible. Ligand binding was monitored by STM on a single

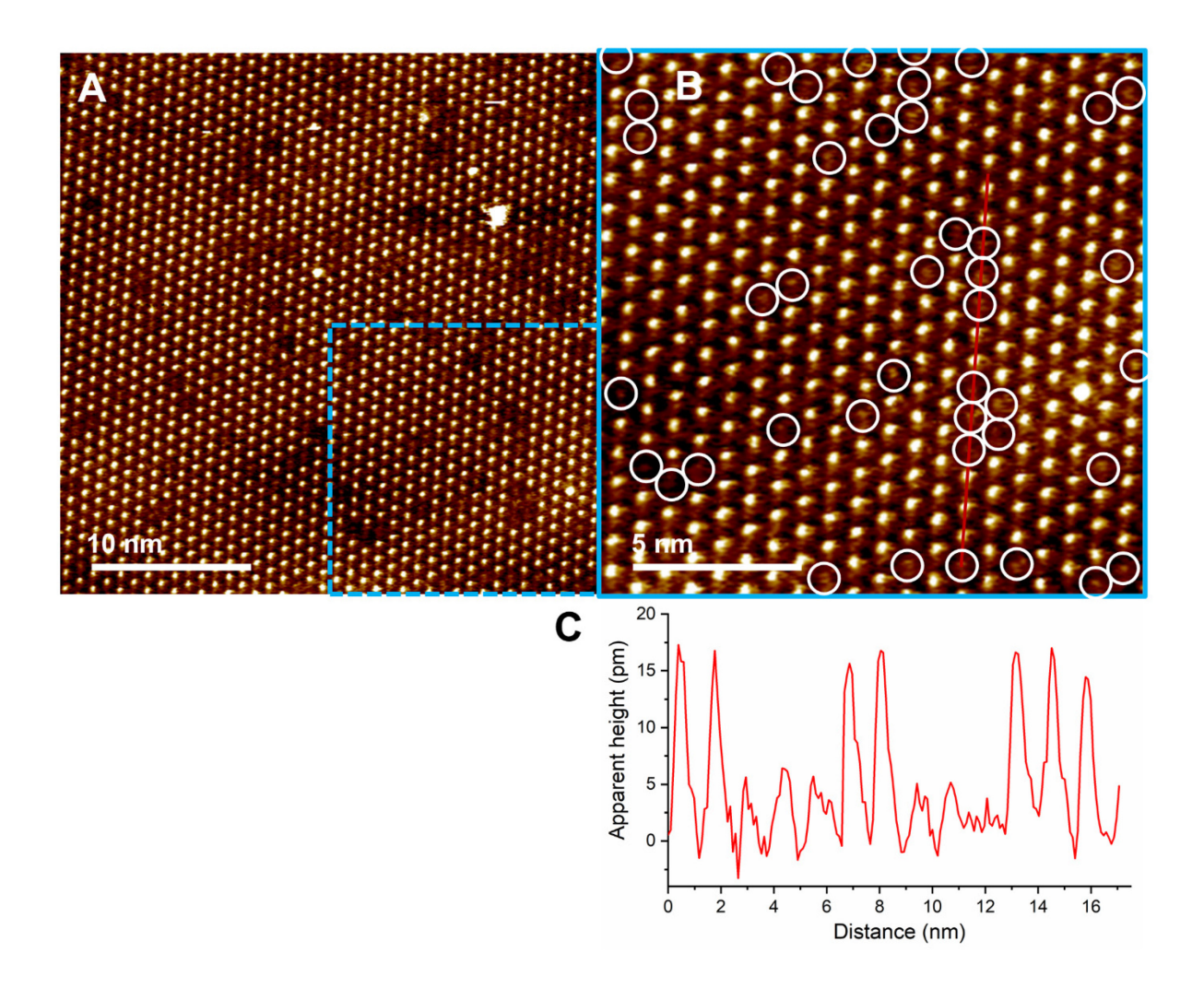


Figure 2. A) A representative STM image of CoOEP on HOPG, in phenyloctane/toluene, after the addition of PhIm. Data was acquired using a bias voltage of +0.600 V and 10 pA setpoint, under argon atmosphere, at room temperature. B) A closer look at a section of A) (blue dashed outline) reveals both bright and dark (circled) molecules. C) The cross-sectional profile (along red line in 2B) supports two populations of molecules being present.

molecule level, by scanning the same area of the sample over time. Sequential STM images revealed molecule blinking' (Figure 3), where molecules were observed to transition from bright to dark and dark to bright. This change in contrast is interpreted as the ligation (bright to dark) and de-ligation (dark to bright) reactions of CoOEP with PhIm. Reversible binding of ligands on surface supported octaethylporphyrins has also been observed for $O_2(g)/CoOEP$ and imidazole/nickel(II) octaethylporphyrin (NiOEP) systems. 36,38 Note that the number of molecules undergoing transitions is low from frame-to-frame in Figure 3, comprising ~ 1 or 2% of the total CoOEP molecules imaged (Table S1). This indicates a relatively long (minutes) mean lifetime for the ligated species.

The observed binding reactions of O_2 to $CoOEP^{36}$ and imidazole to $NiOEP,^{38}$ and the inferred reaction of O_2 with $CuOEP,^{37}$ did not occur in solution and required their respective porphyrins to be surface supported for the reactions to occur. In contrast, UV-visible spectra obtained of a solution of CoOEP in toluene before and after PhIm was added (Supporting Information, Figure S3) show that PhIm

does bind to CoOEP in solution. Prior to PhIm addition, the spectrum of CoOEP was similar to those previously reported, 36,43 with a prominent Soret band at 394 nm and Q-bands at 519 nm and 553 nm. Upon addition of PhIm to the CoOEP solution, a shoulder appeared $\sim\!420$ nm which is interpreted as due to the CoOEP–PhIm adduct. This result is similar to previous observations of nitrogen base binding to CoOEP, 43 where addition of imidazole to a solution of CoOEP in dichloromethane resulted in the formation of a 1:1 CoOEP–imidazole complex and its related band at 418 nm.

Binding of PhIm to the CoOEP monolayer is cooperative. Upon further inspection of STM images of the PhIm/CoOEP/HOPG system, the distribution of dark ligand-bound molecules was noticeably clustered in many cases. To quantify this apparent clustering, an analysis of the relative proportion of the number of dark CoOEP neighbors (for each dark molecule) was undertaken. A similar analysis has been previously presented in the case of O_2 binding to manganese porphyrins.^{34,35} In the those

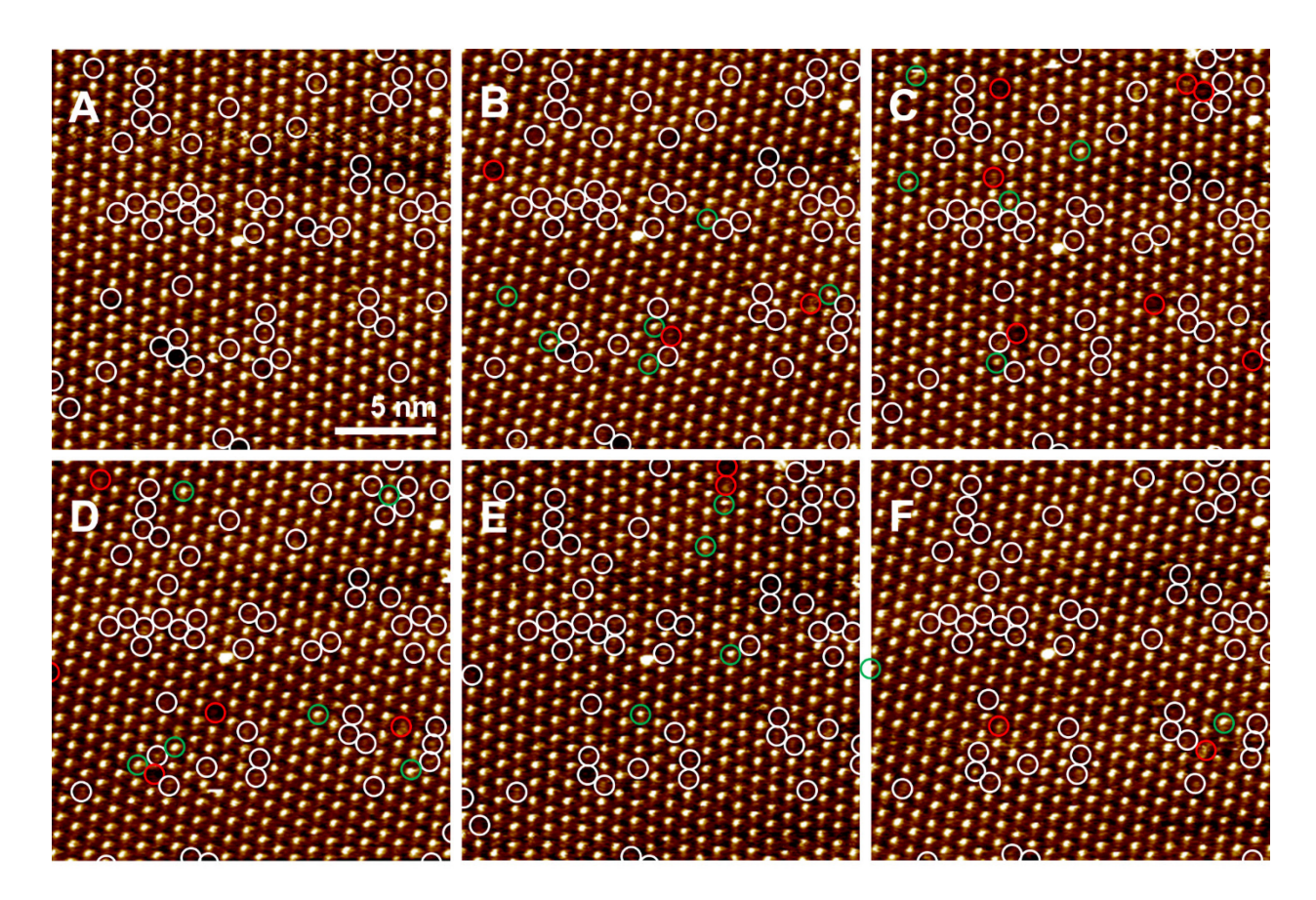


Figure 3. Sequential STM images collected every 1 min 25 sec of CoOEP/HOPG in phenyloctane/toluene (beginning at 1 h 45 min after PhIm addition) demonstrate molecule 'blinking'. Ligand bound molecules (dark) from the first frame (A), or those still bound from the previous frame, are indicated by white circles. Molecules that have de-ligated from the previous frame (now bright) are denoted by green circles, and newly PhIm bound CoOEP (now dark) are indicated by red circles. Average fraction of bound porphyrins (p) across images A–F is 0.113 ± 0.003 .

cases, the non-random distribution was attributed to the 0 atoms produced by the dissociation of 0_2 binding to the nearest available Mn site. This was not considered to be cooperative in the sense that the energy of binding was not considered.

If ligand binding was truly random, where binding to one site on the monolayer did not influence subsequent ligand binding at neighboring molecules, the proportion of dark CoOEP (ligand-bound) molecules (*p*) with *k*-dark neighbors would follow a binomial distribution given by

$$f_k = {6 \choose k} p^k (1 - p)^{6-k}$$

To determine the experimental distribution of k-dark nearest neighbors, a typical analysis is briefly outlined as follows. 50 nm \times 50 nm STM images of the PhIm/CoOEP/HOPG system were analyzed (\sim 1600 CoOEP molecules, on average, per image). For each image, dark molecules were identified and counted to determine p, and the number of dark neighbors for each molecule was counted and tabulated. From this data the fraction of molecules with each k number of dark neighbors was calculated (i.e. for k=0,1,2,3,4,5, and 6, given that CoOEP organized in a hexagonal lattice has six neighboring CoOEP molecules). Full details regarding analysis methods are provided in the Supporting Information.

A representative neighbor analysis and result is provided in Figure 4 and shows a greater number of dark (PhImbound) CoOEP with 2 or more dark nearest neighbors than otherwise expected, assuming a random (binomial) distribution. The summary histogram of experimental and theoretical distribution of k-dark nearest neighbors in Figure 4C shows a larger fraction of dark nearest neighbors for k = 2, 3, 4, and 5 compared with the theoretical prediction, shifting the distribution towards higher numbers of neighbors with bound PhIm. This result suggests that the binding of PhIm to a given CoOEP molecule on HOPG increases the chance that PhIm will bind to a neighboring molecule in the monolayer—in essence, that the binding of PhIm to CoOEP is cooperative.

A summary of our STM results across multiple samples and images is presented as a series of scatterplots in Figure 5. Plotting the ratio of experimental fraction and theoretical fraction of k-dark nearest neighbors allows us to compare the binding of PhIm to CoOEP if p varies. (calculation details provided in Supporting Information). If the distribution of k-dark nearest neighbors was random, we would expect the calculated ratios to be close to 1, as the experimental fraction of k-dark nearest neighbors \simeq theoretical fraction. This, however, is not what we observe. Instead, the majority of data points for k = 2 are above 1, meaning a larger amount of molecules with 2 dark nearest

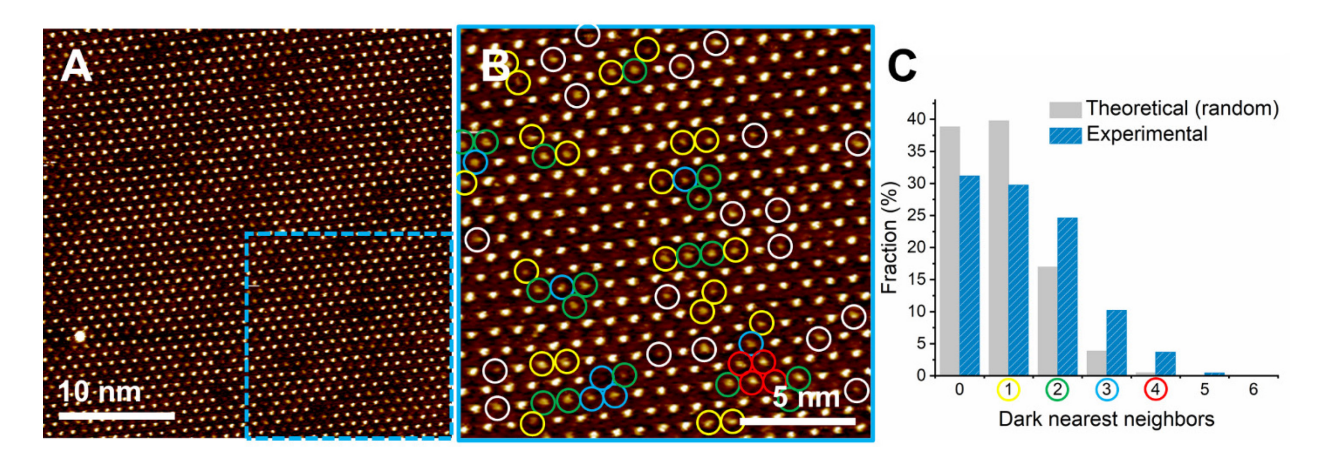


Figure 4. A) Typical image of PhIm binding to the CoOEP monolayer, with the fraction of dark molecules (for this image) of p = 0.146. B) Enlarged section of A): Dark (ligand-bound) molecules are circled, with colors indicating the number of dark nearest neighbors observed for that particular molecule (white = 0, yellow = 1, green = 2, blue = 3, red = 4). C) Histogram comparing the theoretical distribution of dark nearest neighbors (for p = 0.146) and experimentally observed distribution for ligand-bound molecules in A).

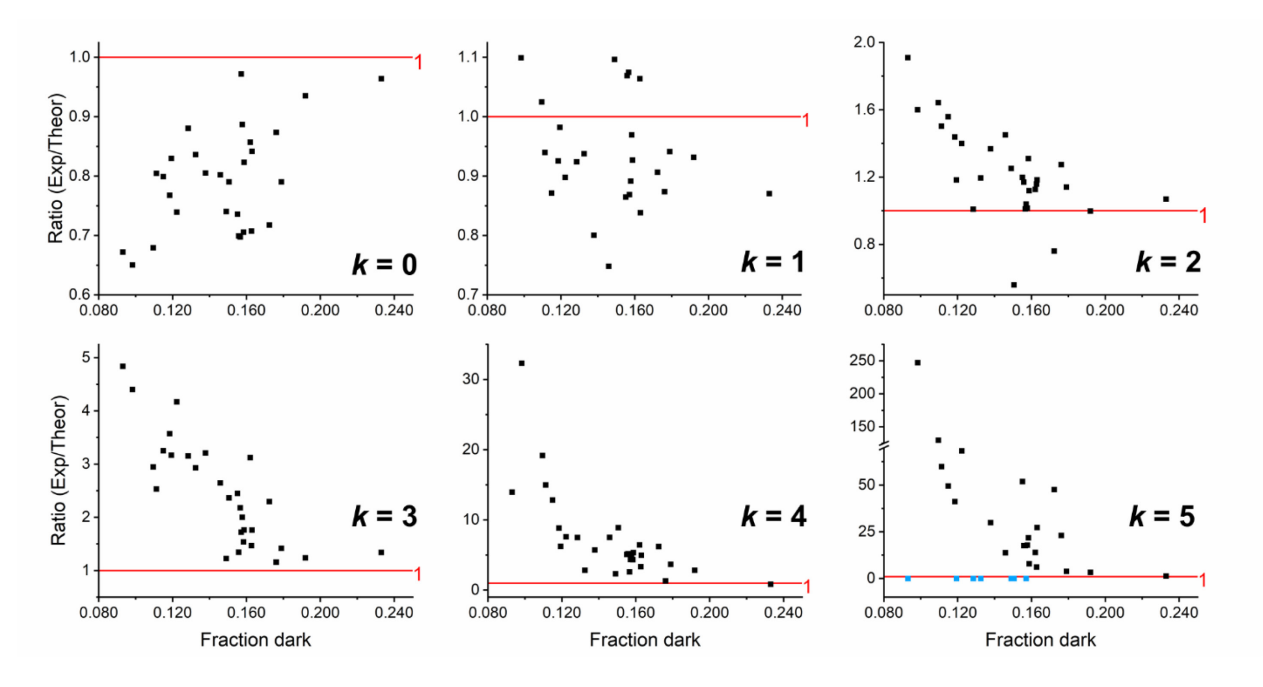


Figure 5. Ratio of experimental and theoretical fractions of k-dark nearest neighbors versus the fraction of total dark molecules (p). Red line in scatterplots indicates unity, where experimental and theoretical fractions of k-dark nearest neighbors would be equivalent. Points in blue denote images where no molecules were observed with the indicated k-dark nearest neighbors.

neighbors are observed than predicted. For k=3, 4, and 5 almost all of our data has a ratio greater than 1, showing a greater proportion of molecules with k-dark nearest neighbors observed versus theory. These results strengthen the conclusion that the binding of PhIm to CoOEP is cooperative in nature. Note that, because of the low coverages observed, very few images had cases where molecules had 6 dark nearest neighbors, therefore we cannot conclude that this trend continues for k=6. The theoretical incidence of ligand bound CoOEP with 6-dark nearest neighbors at even the higher values of p observed (e.g. p=0.233) is extremely small (e.g. $f_6(p=0.233)=0.0160$ %), compared with k=5 where $f_5(p=0.233)=0.315$ % (a $\sim 20 \times 10^{-2}$ increase). For an image with ~ 1600 CoOEP molecules,

these numbers translate into essentially 0 (0.0596) dark molecules predicted with 6-dark neighbors (k=6), and only 1 dark molecule (1.174) with 5-dark neighbors (k=5) per image. Therefore, the low population of neighbors observed for k = 6 is expected.

It is predicted that if the fraction of bound ligands (p) changes, the distribution of ligand-bound neighbors should also change to reflect the change in population. This change in distribution is easily visualized in Figure S4 (Supporting Information), where the theoretical fraction (%) of k-dark nearest neighbors varies with the fraction of dark molecules. In the experimental data (Figure S4), as the overall fraction of dark molecules varies ($p_{min} = 0.0930$,

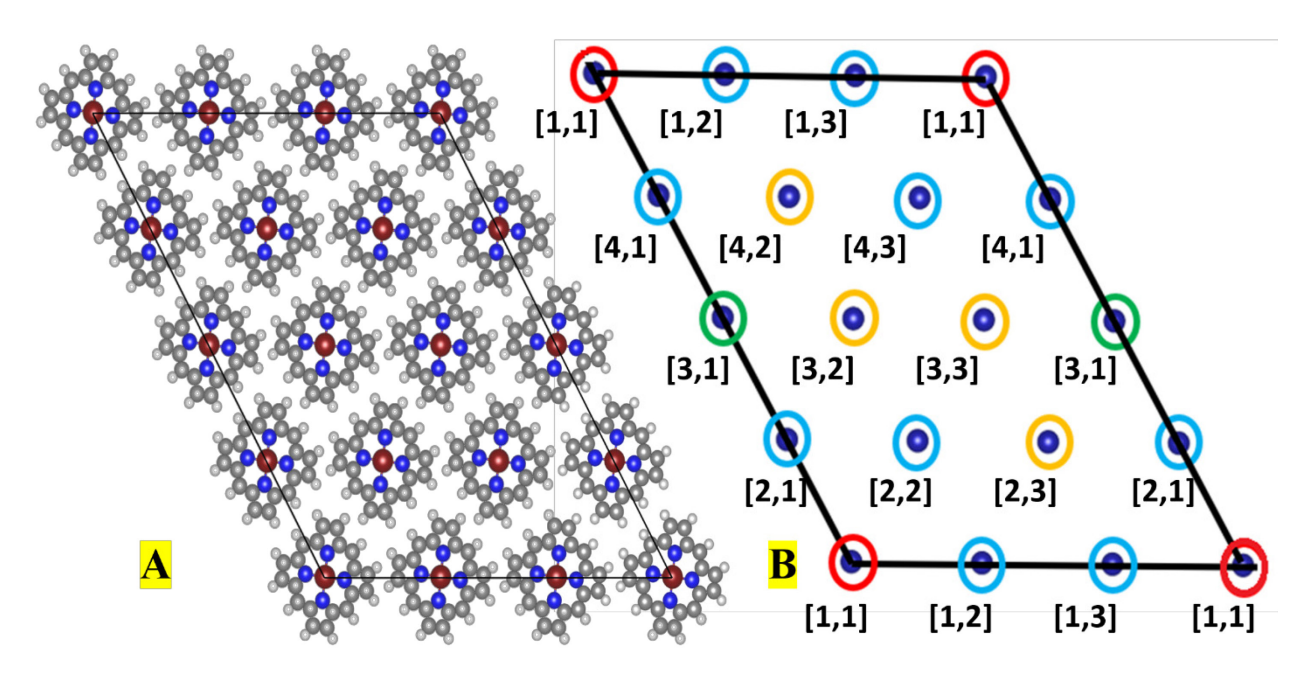


Figure 6. A) Optimized structure CoP/HOPG in 3×4×1 supercell geometry. The HOPG surface is masked for clarity. The unitcell boundaries are represented by black lines. Atom colors: Cobalt-brown, porphyrin and imidazole carbons-grey, nitrogen-blue, hydrogen-white. B) A grid model for 3×4×1 supercell of Co-porphyrin on HOPG. Each dark blue sphere represents a porphyrin molecule. Considering that the red circle represents a first porphyrin bound to PhIm, the other circles (blue, green, yellow) represent equally spaced positions (by color) with respect to the red circle. The numbers in the square brackets represent positions for each Co-porphyrin molecule inside a 3×4×1 supercell.

 $p_{\rm max}$ = 0.233) the preference for two or more dark neighbors is maintained. That is, across a range of p the experimental fraction of k-dark nearest neighbors is higher than predicted for k = 2, 3, 4, and 5, and correspondingly lower for k = 0 and 1.

Computational results. To better understand the cooperative binding behavior of PhIm ligation to Co porphyrins on HOPG, we performed plane-wave (PW) DFT calculations on selective PhIm/Co-porphyrin/HOPG systems. Our goal for PW-DFT simulations is to determine if cooperativity can be observed through DFT calculations and if so, which parameters can be used to explain this phenomenon. A review by Mahadevi and Sastry¹⁷ details various publications where DFT calculations were used to study cooperativity in molecules. In all these studies, the binding energies between various kinds of molecular moieties are used as parameters to understand cooperativity. Our group used PW-DFT and intermolecular interaction energies of coronene on Au(111) and HOPG surfaces to determine cooperativity.78 It was shown that desorption of coronene on Au(111) is cooperative, while on HOPG, it is not. In the current PW-DFT simulations we will use PhIm binding energies obtained from variably covered PhIm/Coporphyrin/HOPG interfaces to show cooperativity.

The cooperative binding phenomenon was studied using $3\times4\times1$ supercells (Figure 6) of the optimized PhIm/Coporphyrin/HOPG systems. A detailed explanation for choosing $3\times4\times1$ supercell and the respective starting geometries used, can be found in the Supporting Information section 3.2. While STM experiments were performed with Co(II) octaethylporphyrin (CoOEP) monolayers, we used both CoOEP and Co(II) porphine (CoP, Figure 1A) monolayers for studying cooperativity. Computations on

CoOEP/HOPG turn out to be twice as expensive (Supporting Information section 3.2) as CoP/HOPG interfaces, yet, no significant differences were observed in the cooperative binding behavior of PhIm ligands (Supporting Information section 3.4). Considering the computational costs, most of our cooperativity studies were performed using variably covered PhIm on the CoP/HOPG interface in a 3×4×1 supercell (Figure 6).

How to model cooperativity with 3×4×1 supercell. We have shown that PhIm binding is cooperative from STM experiments using nearest dark (PhIm bound) neighbor analysis (Figure 4). The basis for this analysis is counting the number of adjacent PhIm bound CoOEP molecules in each STM image. Since CoOEP adsorbs in a hexagonal symmetry on HOPG surface, each CoOEP molecule has 6 nearest CoOEP neighbors. So, if a CoOEP is bound to PhIm (dark), its six nearest neighbors might have been bound or unbound. Since we observed more dark nearest neighbors than predicted for a random distribution, positive cooperativity is attributed to PhIm binding. We can perform an energetic analysis of nearest neighbors with a 3×4×1 supercell of CoP/HOPG (Figure 6A), which has 12 molecules inside the periodic unitcell. With this choice of cell and a distribution of occupancies multiple permutations of partial to full PhIm coverage can be achieved. While STM experiments consider only the nearest (molecule adjacent) neighbor, PW-DFT calculations consider far neighbors as well (vide infra).

A simpler version of the 3×4×1 supercell structure is shown in Figure 6B, where each circle represents a single porphyrin molecule. One should note there will be only 12 complete circles inside the boundary of the supercell. For example, the red circle is indicative of just one porphyrin

Table 1. Selected geometries for modeling cooperativity using 3×4×1 supercell of Co-Porphyrin/HOPG. For each geometry number (#), the number and position of PhIm ligands is given.

Geometry #	Description	# of Ligands	Positions bound †
1	No bound porphyrins	0	0
2	1 bound porphyrin	1	[1,1]
3	2 bound farthest porphyrins	2	[1,1], [3,1]
4	2 bound far porphyrins	2	[1,1], [2,3]
5	2 bound nearest porphyrins	2	[1,1], [1,2]
6	3 bound nearest porphyrins	3	[1,1], [1,2], [2,1]
7	4 bound nearest porphyrins	4	[1,1], [1,2], [2,1], [2,2]
8	Full monolayer	12	all

[†]Refer to Figure 6B for corresponding positions of bound PhIm molecules in each geometry.

molecule inside the boundary of the unitcell and hence labeled [1,1] in all locations of Figure 6B. Considering only one PhIm molecule being bound to the red [1,1] circle, one can observe three types of unique neighbors colored in blue, green and yellow circles (Figure 6B, S7). Note that all the blue circles are equidistant (11.26 Å in CoP/HOPG) from the red circle and are nearest neighbors. The yellow circles are the next nearest neighbors (19.49 Å in CoP/HOPG) to the red circle followed by green (22.51 Å in CoP/HOPG). Figure S7 shows the intermolecular distances between selected neighbors in a 3×4×1 supercell. Hence for example, considering the red circle is bound with PhIm, if a second PhIm molecule is bound to the blue circle, it means two nearest neighbors are bound. On the other hand, if a red and a green circle are bound to PhIm, then two non-nearest neighbors are bound. While STM experiments consider only the nearest (molecule adjacent) neighbor, PW-DFT calculations consider far neighbors as well. Multiple combinations of bound vs. unbound porphyrin molecules can be found. If the supercell size is bigger than 3×4×1 even more combinations can be achieved.

Due to computational limitations, we selected a set of 8 geometries (Table 1) representing partial to full PhIm coverage of CoP/HOPG interface. These selected geometries present a cumulative representation of nearest neighbor analysis carried out with STM images (Figure 4). In Table 1, note that all the selected geometries are with reference to the corner porphyrin (red circle in Figure 6B) of the unitcell. The 1st geometry in Table 1 refers to no bound porphyrins. Starting from the 2nd geometry, considering the red circle, [1,1] position (Figure 6B) is always bound in any given geometry, filling PhIm with near or far neighbors is listed. The selection of the geometries is based on number of nearest or farthest neighbors within the confines of the 12-molecule unit cell. All the geometries listed in Table 1 are fully relaxed with the bottom layer of HOPG frozen. Due to computational cost, all geometries in Table 1 are optimized using CoP as the adlayer while geometries #1, #2, #5 are also optimized with CoOEP adlayer. Sample pictures of optimized geometries #2, #4, #5, #7 (Table 1) with CoP adlayer are shown in Figure S8.

PhIm binding energies. Figure 7 shows the binding energies of PhIm ligand to CoP/HOPG system for the seven selected (Table 1, Figure 6B) geometries. The method for

obtaining the binding energies is detailed in section 3.3 of the Supporting Information. Note that the computed binding energies are more qualitative than quantitative because the computations are performed in vacuum and are missing components like heats of solution, sublimation, and dewetting⁷⁹ of HOPG, PhIm and CoP (in 1phenyloctane) that are present in the STM experiments. Additionally, while vdW-DF functionals are good qualitatively for porphyrin surface systems, their accuracy in determining the binding/adsorption energies is limited. 38,80,81 The x-axis in Figure 7, represents two numbers for each geometry. First, total number of PhIm molecules in the given geometry and second, the number of nearest neighbors bound with PhIm. A striking characteristic of this plot (Figure 7) is that binding energy of PhIm increases as the number of nearest PhIm bound CoP molecules increases. This steady increase in binding energy of individual PhIm molecules is representative of the positive cooperativity which matches with our STM observations.

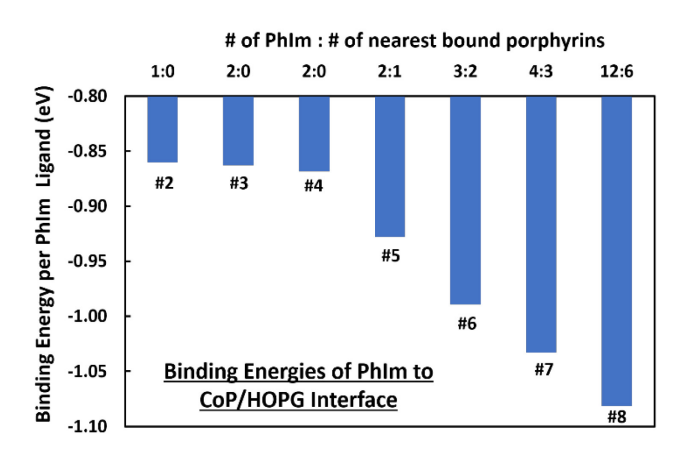


Figure 7. Binding energies of each PhIm ligand to CoP/HOPG with variable PhIm coverage. The geometries representing each bar denoted by a number (#) can be found using Figure 6 and Table 1.

In the CoP/HOPG system, the nearest neighbors are separated by 11.3 Å and the next nearest molecule is spaced by 19.5 Å, followed by 22.5 Å (Figure S7). So, in a PhIm/CoP/HOPG interface with 2 PhIm molecules, if the separation distance between two bound CoP molecules is 11.3 Å, the binding energy per PhIm molecule is 0.93 eV

(#5 in Figure 7), which is 70 meV higher than next nearest CoP molecules (#4 in Figure 7) separated by 19.5 Å. Additionally, the binding energy of singly bound PhIm molecule (#2 in Figure 7) is similar to far spaced PhIm molecules (#3 and #4 in Figure 7) These results indicate that binding energies are really sensitive to separation distance between molecules on the monolayer.

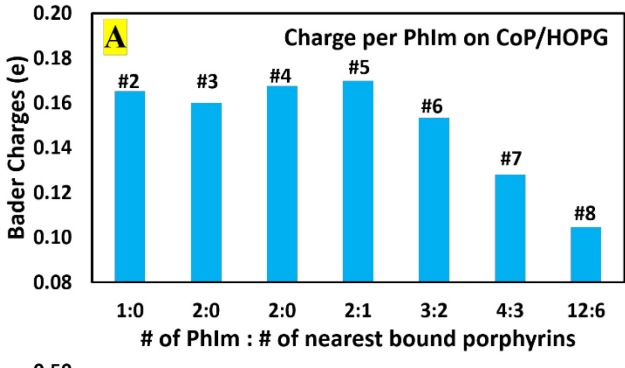
To determine the role of CoP vs. HOPG substrate toward cooperative binding, we performed additional calculations on selected geometries without the HOPG substrate. In this set of calculations, the HOPG substrate was completely removed while the orientation of CoP monolayer from HOPG substrate is kept intact. Further details of the geometries and optimizations are presented in the Supporting Information section 3.5. From this analysis it was found that in the absence of the graphite support having nearest PhIm bound CoP neighbors destabilizes the binding strength of PhIm to CoP. Thus, the HOPG substrate is necessary to observe positive cooperativity in the PhIm/CoP/HOPG systems.

We found that PhIm binding to CoP involves a complex set of interactions based on whether the CoP molecule is part of a monolayer or not on the HOPG substrate. For example, if PhIm is bound to isolated CoP on HOPG (Figure S10-A) with no intermolecular interactions, the binding energy is -1.08 eV. For a similar isolated CoP molecule without the HOPG substrate (Figure S10-B), the PhIm binding energy is -0.94 eV. This indicates that HOPG increases PhIm binding energy by about 140 meV. Moreover, if PhIm is bound to the CoP monolayer, the binding is positively cooperative with HOPG (Figure 7) and negatively cooperative without HOPG (Figure S9). This indicates that dense molecular packing of CoP is also critical to observe cooperativity.

To understand this complex behavior of PhIm binding cooperativity, we studied Bader charges of PhIm/CoP geometries with and without HOPG. The corresponding Bader charges for each component (PhIm, CoP and HOPG) are depicted in Figure 8 (PhIm) and Figure S11 (CoP and HOPG). Some significant observations from these plots are that with HOPG present, PhIm (Figure 8A) acts as charge donor, CoP (Figure S11-A) a charge acceptor, and HOPG (Figure S11-E) charge donor except at high PhIm coverage (#8 in Figure S11-E). As PhIm coverage increases (from geometries #2 to #8), the donating capacity of each PhIm decreases considerably (Figure 8A) while accepting capacity of CoP monolayer decreases mildly (Figure S11-A) because the accepting capacity of HOPG increases significantly (Figure S11-E). In other words, HOPG starts as a donor of charge at no to low PhIm coverage, while turning out to be an acceptor at high PhIm coverage.

Without the HOPG substrate, PhIm (Figure 8B) acts as charge donor and CoP (Figure S11-B) as charge acceptor, except at high PhIm coverage. For example, at full coverage, PhIm (#8 in Figure 8B) acts as an acceptor while CoP monolayer (Figure S11-B) acts as a donor. As PhIm coverage increases (from geometries #2 to #8), the donating capacity of each PhIm decreases considerably (Figure 8B) while accepting capacity of CoP monolayer also decreases significantly (Figure S11-B). In other words, the CoP monolayer without the HOPG substrate ceases to take any elec-

tronic charge from PhIm ligand at high coverage and instead acts as a charge donor.



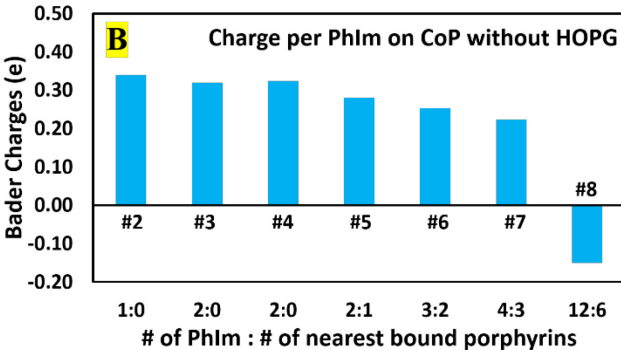


Figure 8. Bader charges of each PhIm molecule in (A) PhIm/CoP/HOPG and (B) PhIm/CoP interfaces. The geometries representing each bar denoted by a number (#) can be found using Figure 6 and Table 1.

There is also an entropic factor to be considered. Because the cooperative assembly is more ordered than the random one, there is a net negative entropy associated with the cooperative adlayer formation. The maximum possible value of this term is the negative of the configurational entropy of the random lattice gas.⁸² For a coverage of p=0.11, this amounts to a contribution less than +10 meV to ΔG . Since the stabilization energy of the cooperative assembly is computed to be of the order of 50 to 100 meV, cooperative behavior is still expected.

CONCLUSIONS

For the first time, a combined experimental and theoretical approach has been developed and applied to study cooperative effects at interfaces for simple porphyrin systems. We have shown that PhIm binds to CoOEP both in solution and when CoOEP is supported on HOPG. The binding reaction of PhIm to the CoOEP monolayer was followed by STM and found to be dynamic and reversible. Presence of the ligand adduct was confirmed even after several days of repeated sample imaging. Positive cooperativity was established for PhIm binding to CoOEP on HOPG by quantifying ligand binding events observed by STM and comparing these results to random distributions. Binding events were not mutually independent, as the binding of PhIm to CoOEP increased the probability of neighboring CoOEP to bind PhIm. Across a fairly wide range of p (fraction of ligand-bound CoOEP) there was a greater amount of ligandbound CoOEP with two or more bound neighbors than expected and a general shift in the experimental neighbor distribution toward higher values of *k*.

These experimental results were supported by DFT calculations that show an increase in binding energy per PhIm ligand as the number of nearest bound porphyrins increases, and as separation distance decreases between bound molecules in the monolayer. Determination of binding energies and Bader charge analysis of systems without HOPG present demonstrated that interactions of the system with HOPG is key in promoting these cooperative interactions. These results are significant to those who wish to use porphyrins for materials applications, particularly as templates for nanoscale assembly, or as models of natural systems.

Given the apparent dependence of the substrate in modulating cooperative interactions, a natural extension of this work will be to investigate different substrates to determine their impact on cooperativity. We have noted that separation distance affects cooperative interactions between single CoOEP molecules. Would separation distance have the same effect in multimeric porphyrin systems? Electronic properties of fused porphyrins or porphyrin oligomers can vary dramatically from the monomer species.83,84 Furthermore, interporphyrin electronic communication between porphyrin receptors is possible and can influence ligand binding and cooperative effects. Negative cooperativity has been observed in the binding of 4,4'bipyridine to a cyclic dimer and of pyridine to fused zinc porphyrins,85 attributed to electronic coupling between binding sites. Understanding the nature of these electronic effects is especially important for multi-site receptor, catalysis, and sensing applications. Our investigation forms a basis for future research that will investigate these questions. As we look to further understand biological processes and use our understanding of natural systems to create synthetic ones, cooperativity remains an important consideration.

ASSOCIATED CONTENT

Supporting Information. Additional experimental details and methods; STM image of CoOEP prior to PhIm addition; STM images showing stability of CoOEP monolayer and adduct over time, transition statistics for 'blinking' of CoOEP in Figure 3; UV-visible spectra of CoOEP and CoOEP/PhIm solutions; experimental and theoretical fractions of molecules with *k*-dark nearest neighbors versus *p*; details regarding computational modeling. This material is available free of charge via the Internet at http://pubs.acs.org.

AUTHOR INFORMATION

Corresponding Authors

* Ursula Mazur – Email: umazur@wsu.edu; K.W. Hipps – Email: hipps@wsu.edu

ACKNOWLEDGMENTS

This material is based upon work supported by the National Science Foundation under Grant No. CHE-1800070. Computational work is performed using resources from the Center for Institutional Research Computing (CIRC) at Washington State University (WSU). This work also used Extreme Science and Engineering Discovery Environment (XSEDE), Request No.

CHE190102, which is supported by National Science Foundation grant number ACI-1548562. The authors gratefully acknowledge Kristen N. Johnson for obtaining UV-visible spectra of CoOEP and CoOEP/PhIm solutions.

REFERENCES

- (1) Li, Y.; Wang, Y.; Huang, G.; Gao, J. Cooperativity Principles in Self-Assembled Nanomedicine. *Chem. Rev.* **2018**, *118*, 5359–5391.
- (2) Skoge, M.; Meir, Y.; Wingreen, N. S. Dynamics of Cooperativity in Chemical Sensing among Cell-Surface Receptors. *Phys. Rev. Lett.* **2011**, *107*, 178101.
- (3) Pauling, L. The Oxygen Equilibrium of Hemoglobin and Its Structural Interpretation. *Proc. Natl. Acad. Sci. U.S.A.* **1935**, *21*, 186–191.
- (4) Ercolani, G.; Schiaffino, L. Allosteric, Chelate, and Interannular Cooperativity: A Mise au Point. *Angew. Chem., Int. Ed.* **2011**, *50*, 1762–1768.
- (5) Goodey, N. M.; Benkovic, S. J. Allosteric Regulation and Catalysis Emerge via a Common Route. *Nat. Chem. Biol.* **2008**, *4*, 474–482.
- (6) Whitty, A. Cooperativity and Biological Complexity. *Nat. Chem. Biol.* **2008**, *4*, 435–439.
- (7) Rest, C.; Kandanelli, R.; Fernández, G. Strategies to Create Hierarchical Self-Assembled Structures via Cooperative Non-Covalent Interactions. *Chem. Soc. Rev.* **2015**, *44*, 2543–2572.
- (8) Chandra, P.; Jonas, A. M.; Fernandes, A. E. Spatial Coordination of Cooperativity in Silica-Supported Cu/TEMPO/Imidazole Catalytic Triad. *ACS Catal.* **2018**, *8*, 6006–6011.
- (9) Li, L.; Hu, J.; Shi, X.; Shao, Y.; Song, F. Lipid Rafts Enhance the Binding Constant of Membrane-Anchored Receptors and Ligands. *Soft Matter* **2017**, *13*, 4294–4304.
- (10) Groizard, T.; Papior, N.; Le Guennic, B.; Robert, V.; Kepenekian, M. Enhanced Cooperativity in Supported Spin-Crossover Metal-Organic Frameworks. *J. Phys. Chem. Lett.* **2017**, *8*, 3415–3420.
- (11) Kipgen, L.; Bernien, M.; Ossinger, S.; Nickel, F.; Britton, A. J.; Arruda, L. M.; Naggert, H.; Luo, C.; Lotze, C.; Ryll, H. et al. Evolution of Cooperativity in the Spin Transition of an Iron(II) Complex on a Graphite Surface. *Nat. Commun.* **2018**, *9*, 1–8.
- (12) Hunter, C. A.; Anderson, H. L. What Is Cooperativity? *Angew. Chem., Int. Ed.* **2009**, *48*, 7488–7499.
- (13) Rong, C.; Zhao, D.; Yu, D.; Liu, S. Quantification and Origin of Cooperativity: Insights from Density Functional Reactivity Theory. *Phys. Chem. Chem. Phys.* **2018**, *20*, 17990–17998.
- (14) Rong, C.; Zhao, D.; Zhou, T.; Liu, S.; Yu, D.; Liu, S. Homogeneous Molecular Systems Are Positively Cooperative, but Charged Molecular Systems Are Negatively Cooperative. *J. Phys. Chem. Lett.* **2019**, *10*, 1716–1721.
- (15) Vijay, D.; Zipse, H.; Sastry, G. N. On the Cooperativity of Cation- π and Hydrogen Bonding Interactions. *J. Phys. Chem. B* **2008**, *112*, 8863–8867.
- (16) Pérez, C.; Zaleski, D. P.; Seifert, N. A.; Temelso, B.; Shields, G. C.; Kisiel, Z.; Pate, B. H. Hydrogen Bond Cooperativity and the Three-Dimensional Structures of Water Nonamers and Decamers. *Angew. Chem., Int. Ed.* **2014**, *53*, 14368–14372.
- (17) Mahadevi, A. S.; Sastry, G. N. Cooperativity in Noncovalent Interactions. *Chem. Rev.* **2016**, *116*, 2775–2825.
- (18) Sundberg, R. J.; Martin, R. B. Interactions of Histidine and Other Imidazole Derivatives with Transition Metal Ions in Chemical and Biological Systems. *Chem. Rev.* **1974**, *74*, 471–517.
- (19) Chen, S.-S. The Roles of Imidazole Ligands in Coordination Supramolecular Systems. *CrystEngComm* **2016**, *18*, 6543–6565.
- (20) Porath, J. Immobilized Metal Ion Affinity Chromatography. *Protein Expression and Purification* **1992**, *3*, 263–281.
- (21) Senge, M. O.; MacGowan, S. A.; O'Brien, J. M. Conformational Control of Cofactors in Nature the Influence of Protein-Induced Macrocycle Distortion on the Biological Function of Tetrapyrroles. *Chem. Commun.* **2015**, *51*, 17031–17063.

- (22) García-Sánchez, M. A.; Rojas-González, F.; Menchaca-Campos, E. C.; Tello-Solís, S. R.; Quiroz-Segoviano, R. I. Y.; Diaz-Alejo, L. A.; Salas-Bañales, E.; Campero, A. Crossed and Linked Histories of Tetrapyrrolic Macrocycles and Their Use for Engineering Pores within Sol-Gel Matrices. *Molecules* **2013**, *18*, 588–653.
- (23) Shapleigh, J. P.; Hosler, J. P.; Tecklenburg, M. M.; Kim, Y.; Babcock, G. T.; Gennis, R. B.; Ferguson-Miller, S. Definition of the Catalytic Site of Cytochrome c Oxidase: Specific Ligands of Heme a and the Heme a_3 -Cu_B Center. *Proc. Natl. Acad. Sci. U.S.A.* **1992**, *89*, 4786–4790.
- (24) Kranz, R. G.; Richard-Fogal, C.; Taylor, J.-S.; Frawley, E. R. Cytochrome *c* Biogenesis: Mechanisms for Covalent Modifications and Trafficking of Heme and for Heme-Iron Redox Control. *Microbiol. Mol. Biol. Rev.* **2009**, *73*, 510–528.
- (25) Vlasie, M.; Chowdhury, S.; Banerjee, R. Importance of the Histidine Ligand to Coenzyme B12 in the Reaction Catalyzed by Methylmalonyl-CoA Mutase. *J. Biol. Chem.* **2002**, *277*, 18523–18527.
- (26) Muralidhara, B. K.; Negi, S.; Chin, C. C.; Braun, W.; Halpert, J. R. Conformational Flexibility of Mammalian Cytochrome P450 2B4 in Binding Imidazole Inhibitors with Different Ring Chemistry and Side Chains. Solution Thermodynamics and Molecular Modeling. *J. Biol. Chem.* **2006**, *281*, 8051–8061.
- (27) Basudhar, D.; Madrona, Y.; Kandel, S.; Lampe, J. N.; Nishida, C. R.; de Montellano, P. R. O. Analysis of Cytochrome P450 CYP119 Ligand-Dependent Conformational Dynamics by Two-Dimensional NMR and X-Ray Crystallography. *J. Biol. Chem.* **2015**, *290*, 10000–10017.
- (28) Paolesse, R.; Nardis, S.; Monti, D.; Stefanelli, M.; Di Natale, C. Porphyrinoids for Chemical Sensor Applications. *Chem. Rev.* **2017**, *117* (4), 2517–2583.
- (29) Zhang, W.; Lai, W.; Cao, R. Energy-Related Small Molecule Activation Reactions: Oxygen Reduction and Hydrogen and Oxygen Evolution Reactions Catalyzed by Porphyrin- and Corrole-Based Systems. *Chem. Rev.* **2017**, *117*, 3717–3797.
- (30) Barona-Castaño, J. C.; Carmona-Vargas, C. C.; Brocksom, T. J.; de Oliveira, K. T. Porphyrins as Catalysts in Scalable Organic Reactions. *Molecules* **2016**, *21*, 310.
- (31) Zhao, L.; Qu, R.; Li, A.; Ma, R.; Shi, L. Cooperative Self-Assembly of Porphyrins with Polymers Possessing Bioactive Functions. *Chem. Commun.* **2016**, *52*, 13543–13555.
- (32) Gottfried, J. M. Surface Chemistry of Porphyrins and Phthalocyanines. *Surf. Sci. Rep.* **2015**, *70*, 259–379.
- (33) Hieringer, W.; Flechtner, K.; Kretschmann, A.; Seufert, K.; Auwärter, W.; Barth, J. V.; Görling, A.; Steinrück, H.-P.; Gottfried, J. M. The Surface Trans Effect: Influence of Axial Ligands on the Surface Chemical Bonds of Adsorbed Metalloporphyrins. *J. Am. Chem. Soc.* **2011**, *133*, 6206–6222.
- (34) Hulsken, B.; Van Hameren, R.; Gerritsen, J. W.; Khoury, T.; Thordarson, P.; Crossley, M. J.; Rowan, A. E.; Nolte, R. J. M.; Elemans, J. A. A. W.; Speller, S. Real-Time Single-Molecule Imaging of Oxidation Catalysis at a Liquid-Solid Interface. *Nat. Nanotechnol.* **2007**, *2*, 285–289.
- (35) Murphy, B. E.; Krasnikov, S. A.; Sergeeva, N. N.; Cafolla, A. A.; Preobrajenski, A. B.; Chaika, A. N.; Lübben, O.; Shvets, I. V. Homolytic Cleavage of Molecular Oxygen by Manganese Porphyrins Supported on Ag(111). *ACS Nano* **2014**, *8*, 5190–5198.
- (36) Friesen, B. A.; Bhattarai, A.; Mazur, U.; Hipps, K. W. Single Molecule Imaging of Oxygenation of Cobalt Octaethylporphyrin at the Solution/Solid Interface: Thermodynamics from Microscopy. *J. Am. Chem. Soc.* **2012**, *134*, 14897–14904.
- (37) Hao, Y.; Weatherup, R. S.; Eren, B.; Somorjai, G. A.; Salmeron, M. Influence of Dissolved O_2 in Organic Solvents on CuOEP Supramolecular Self-Assembly on Graphite. *Langmuir* **2016**, *32*, 5526–5531.
- (38) Nandi, G.; Chilukuri, B.; Hipps, K. W.; Mazur, U. Surface Directed Reversible Imidazole Ligation to Nickel(II) Octaethylpor-

- phyrin at the Solution/Solid Interface: A Single Molecule Level Study. *Phys. Chem. Chem. Phys.* **2016**, *18*, 20819–20829.
- (39) Mochida, I.; Suetsugu, K.; Fujitsu, H.; Takeshita, K. Unusual Activity of Carbon Monoxide on Co-Tetraphenylporphyrin Supported by TiO₂ for the Reduction of Nitric Oxide. *J. Chem. Soc., Chem. Commun.* **1982**, No. 3, 166–167.
- (40) den Boer, D.; Li, M.; Habets, T.; Iavicoli, P.; Rowan, A. E.; Nolte, R. J. M.; Speller, S.; Amabilino, D. B.; De Feyter, S.; Elemans, J. A. A. W. Detection of Different Oxidation States of Individual Manganese Porphyrins during Their Reaction with Oxygen at a Solid/Liquid Interface. *Nat. Chem.* **2013**, *5*, 621–627.
- (41) Hipps, K. W.; Mazur, U. Kinetic and Thermodynamic Control in Porphyrin and Phthalocyanine Self-Assembled Monolayers. *Langmuir* **2018**, *34*, 3–17.
- (42) Yoshimoto, S.; Yasunishi, S.; Kawamoto, T. Effect of the Formation of Highly Ordered Platinum(II) Octaethylporphyrin Adlayer on the Surface Reconstruction of Gold and Supramolecular Assembly of Fullerenes. *J. Phys. Chem. C* **2014**, *118*, 29880–29886.
- (43) Tan, Y.; Escorcia, N.; Hyslop, A.; Wang, E. Investigation of Cobalt Porphyrin Doped Polymer Membrane Films for the Optical Sensing of Imidazole and Its Derivatives. *Anal. Chem. Res.* **2015**, *3*, 70–76.
- (44) Hu, C.; An, J.; Noll, B. C.; Schulz, C. E.; Scheidt, W. R. Electronic Configuration of High-Spin Imidazole-Ligated Iron(II) Octaethylporphyrinates. *Inorg. Chem.* **2006**, *45*, 4177–4185.
- (45) Scheidt, W. Robert.; Chipman, D. M. Preferred Orientation of Imidazole Ligands in Metalloporphyrins. *J. Am. Chem. Soc.* **1986**, *108*, 1163–1167.
- (46) Kamm, J. M.; Iverson, C. P.; Lau, W.-Y.; Hopkins, M. D. Axial Ligand Effects on the Structures of Self-Assembled Gallium-Porphyrin Monolayers on Highly Oriented Pyrolytic Graphite. *Langmuir* **2016**, *32*, 487–495.
- (47) Ferreira, Q.; Alcácer, L.; Morgado, J. Stepwise Preparation and Characterization of Molecular Wires Made of Zinc Octaethylporphyrin Complexes Bridged by 4, 4'-Bipyridine on HOPG. *Nanotechnology* **2011**, *22*, 435604.
- (48) Ellis, P. E.; Linard, J. E.; Szymanski, T.; Jones, R. D.; Budge, J. R.; Basolo, F. Axial Ligation Constants of Iron(II) and Cobalt(II) "Capped" Porphyrins. *J. Am. Chem. Soc.* **1980**, *102*, 1889–1896.
- (49) Collman, J. P.; Brauman, J. I.; Doxsee, K. M.; Halbert, T. R.; Hayes, S. E.; Suslick, K. S. Oxygen Binding to Cobalt Porphyrins. *J. Am. Chem. Soc.* **1978**. *100*. 2761–2766.
- (50) KC, C. B.; Lim, G. N.; D'Souza, F. Multi-Modular, Tris(Triphenylamine) Zinc Porphyrin–Zinc Phthalocyanine–Fullerene Conjugate as a Broadband Capturing, Charge Stabilizing, Photosynthetic 'Antenna-Reaction Center' Mimic. *Nanoscale* **2015**, *7*, 6813–6826.
- (51) Liao, M.-S.; Huang, M.-J.; Watts, J. D. Iron Porphyrins with Different Imidazole Ligands. A Theoretical Comparative Study. *J. Phys. Chem. A* **2010**, *114*, 9554–9569.
- (52) Mishra, E.; Worlinsky, J. L.; Gilbert, T. M.; Brückner, C.; Ryzhov, V. Axial Imidazole Binding Strengths in Porphyrinoid Cobalt(III) Complexes as Studied by Tandem Mass Spectrometry. *J. Am. Soc. Mass Spectrom.* **2012**, *23*, 1135–1146.
- (53) Martini, L. A.; Moore, G. F.; Milot, R. L.; Cai, L. Z.; Sheehan, S. W.; Schmuttenmaer, C. A.; Brudvig, G. W.; Crabtree, R. H. Modular Assembly of High-Potential Zinc Porphyrin Photosensitizers Attached to TiO₂ with a Series of Anchoring Groups. *J. Phys. Chem. C* **2013**, *117*, 14526–14533.
- (54) Tran, T. T. H.; Chen, G.-L.; Hoang, T. K. A.; Kuo, M.-Y.; Su, Y. O. Effect of Imidazole on the Electrochemistry of Zinc Porphyrins: An Electrochemical and Computational Study. *J. Phys. Chem. A* **2017**, *121*, 6925–6931.
- (55) Moghadam, M.; Tangestaninejad, S.; Mirkhani, V.; Kargar, H.; Komeili-Isfahani, H. Polystyrene-Bound Imidazole as a Heterogeneous Axial Ligand for Mn(TPP)Cl and Its Use as Hydrocarbon Monooxygenation Catalyst in the Alkene Epoxidation and Alkane

- Hydroxylation with Sodium Periodate under Various Reaction Conditions. *Catal. Comm.* **2005**, *6*, 688–693.
- (56) Yang, J.; Huang, P. A Study of Cobalt(II) Porphyrins on Their Oxygen-Binding Behaviors and Oxygen-Facilitated Transport Properties in Polymeric Membranes. *Chem. Mater.* **2000**, *12*, 2693–2697.
- (57) Walker, F. A.; Lo, M.-W.; Ree, M. T. Electronic Effects in Transition Metal Porphyrins. The Reactions of Imidazoles and Pyridines with a Series of Para-Substituted Tetraphenylporphyrin Complexes of Chloroiron(III). *J. Am. Chem. Soc.* **1976**, *98*, 5552–5560.
- (58) Chang, M. H.; Chang, Y. H.; Kim, N.-Y.; Kim, H.; Lee, S.-H.; Choi, M.-S.; Kim, Y.-H.; Kahng, S.-J. Tuning and Sensing Spin Interactions in Co-Porphyrin/Au with NH₃ and NO₂ Binding. *Phys. Rev. B* **2019**, *100*, 245406.
- (59) Chang, M. H.; Kim, N.-Y.; Chang, Y. H.; Lee, Y.; Jeon, U. S.; Kim, H.; Kim, Y.-H.; Kahng, S.-J. O₂, NO₂ and NH₃ Coordination to Co-Porphyrin Studied with Scanning Tunneling Microscopy on Au(111). *Nanoscale* **2019**, *11*, 8510–8517.
- (60) T. N. Ha, N.; Gopakumar, T. G.; D. C. Yen, N.; Mende, C.; Smykalla, L.; Schlesinger, M.; Buschbeck, R.; Rüffer, T.; Lang, H.; Mehring, M.; Hietschold, M. Ester Formation at the Liquid–Solid Interface. *Beilstein J. Nanotechnol.* **2017**, *8*, 2139–2150.
- (61) Münninghoff, J. A. W.; Elemans, J. A. A. W. Chemistry at the Square Nanometer: Reactivity at Liquid/Solid Interfaces Revealed with an STM. *Chem. Commun.* **2017**, *53*, 1769–1788.
- (62) Oliveira, J.; Bragança, A. M.; Alcácer, L.; Morgado, J.; Figueiredo, M.; Bioucas-Dias, J.; Ferreira, Q. Sparse-Coding Denoising Applied to Reversible Conformational Switching of a Porphyrin Self-Assembled Monolayer Induced by Scanning Tunnelling Microscopy. *J. Microsc.* **2018**, *271*, 98–108.
- (63) Kresse, G.; Furthmüller, J. Efficiency of Ab-Initio Total Energy Calculations for Metals and Semiconductors Using a Plane-Wave Basis Set. *Comput. Mater. Sci.* **1996**, *6*, 15–50.
- (64) Kresse, G.; Hafner, J. Ab Initio Molecular Dynamics for Liquid Metals. *Phys. Rev. B* **1993**, *47*, 558–561.
- (65) Kresse, G.; Joubert, D. From Ultrasoft Pseudopotentials to the Projector Augmented-Wave Method. *Phys. Rev. B* **1999**, *59*, 1758
- (66) Gajdoš, M.; Hummer, K.; Kresse, G.; Furthmüller, J.; Bechstedt, F. Linear Optical Properties in the Projector-Augmented Wave Methodology. *Phys. Rev. B* **2006**, *73*, 045112.
- (67) Blöchl, P. E. Projector Augmented-Wave Method. *Phys. Rev.* B **1994**, *50*, 17953.
- (68) Klimeš, J.; Bowler, D. R.; Michaelides, A. Van der Waals Density Functionals Applied to Solids. *Phys. Rev. B* **2011**, *83*, 195131.
- (69) Becke, A. D. Density-Functional Exchange-Energy Approximation with Correct Asymptotic Behavior. *Phys. Rev. A* **1988**, *38*, 3098.
- (70) Klimeš, J.; Bowler, D. R.; Michaelides, A. Chemical Accuracy for the van der Waals Density Functional. *J. Phys. Condens. Matter* **2009**, *22*, 022201.
- (71) Perdew, J. P.; Burke, K.; Ernzerhof, M. Generalized Gradient Approximation Made Simple. *Phys. Rev. Lett.* **1996**, *77*, 3865.
- (72) Monkhorst, H. J.; Pack, J. D. Special Points for Brillouin-Zone Integrations. *Phys. Rev. B* **1976**, *13*, 5188.
- (73) Chilukuri, B.; Mazur, U.; Hipps, K. W. Effect of Dispersion on Surface Interactions of Cobalt(II) Octaethylporphyrin Monolayer on Au(111) and HOPG(0001) Substrates: A Comparative First Principles Study. *Phys. Chem. Chem. Phys.* **2014**, *16*, 14096–14107
- (74) Jahanbekam, A.; Chilukuri, B.; Mazur, U.; Hipps, K. W. Kinetically Trapped Two-Component Self-Assembled Adlayer. *J. Phys. Chem. C* **2015**, *119*, 25364–25376.
- (75) Adinehnia, M.; Borders, B.; Ruf, M.; Chilukuri, B.; Hipps, K. W.; Mazur, U. Comprehensive Structure–Function Correlation of Photoactive Ionic π -Conjugated Supermolecular Assemblies: An

- Experimental and Computational Study. *J. Mater. Chem. C* **2016**, *4*, 10223–10239.
- (76) Borders, B.; Adinehnia, M.; Chilukuri, B.; Ruf, M.; Hipps, K. W.; Mazur, U. Tuning the Optoelectronic Characteristics of Ionic Organic Crystalline Assemblies. *J. Mater. Chem. C* **2018**, *6*, 4041–4056.
- (77) Zhang, Y. C.; Chilukuri, B.; Hanson, T. B.; Heiden, Z. M.; Lee, D. Y. Connecting Solution-Phase to Single-Molecule Properties of Ni(Salophen). *J. Phys. Chem. Lett.* **2019**, *10*, 3525–3530.
- (78) Chilukuri, B.; Mazur, U.; Hipps, K. W. Cooperativity and Coverage Dependent Molecular Desorption in Self-Assembled Monolayers: Computational Case Study with Coronene on Au (111) and HOPG. *Phys. Chem. Chem. Phys.* **2019**, *21*, 10505–10513.
- (79) Song, W.; Martsinovich, N.; Heckl, W. M.; Lackinger, M. Born-Haber Cycle for Monolayer Self-Assembly at the Liquid-Solid Interface: Assessing the Enthalpic Driving Force. *J. Am. Chem. Soc.* **2013**, *135*, 14854–14862.
- (80) Lee, K.; Murray, É. D.; Kong, L.; Lundqvist, B. I.; Langreth, D. C. Higher-Accuracy van der Waals Density Functional. *Phys. Rev. B* **2010**, *82*, 081101.
- (81) Li, G.; Tamblyn, I.; Cooper, V. R.; Gao, H.-J.; Neaton, J. B. Molecular Adsorption on Metal Surfaces with van der Waals Density Functionals. *Phys. Rev. B* **2012**, *85*, 121409.
- (82) Hill, T.L. *An Introduction to Statistical Thermodynamics;* Addison-Wesley Pub. Co.: Reading, MA, 1960; pp 128.
- (83) Tanaka, T.; Osuka, A. Conjugated Porphyrin Arrays: Synthesis, Properties and Applications for Functional Materials. *Chem. Soc. Rev.* **2015**, *44*, 943–969.
- (84) Mori, H.; Tanaka, T.; Osuka, A. Fused Porphyrinoids as Promising Near-Infrared Absorbing Dyes. *J. Mater. Chem. C* **2013**, *1*, 2500–2519.
- (85) Sato, H.; Tashiro, K.; Shinmori, H.; Osuka, A.; Aida, T. Cyclic Dimer of a Fused Porphyrin Zinc Complex as a Novel Host with Two π -Electronically Coupled Binding Sites. *Chem. Commun.* **2005**, No. 18, 2324–2326.

TOC Graphic

